Topological Materials: Weyl Semimetals

Binghai Yan and Claudia Felser

Department of Solid State Chemistry, Max Planck Institute for Chemical Physics of Solids, 01187 Dresden, Germany; email: yan@cpfs.mpg.de, felser@cpfs.mpg.de

Annu. Rev. Condens. Matter Phys. 2017. 8:337–54

First published online as a Review in Advance on January 11, 2017

The *Annual Review of Condensed Matter Physics* is online at conmatphys.annualreviews.org

https://doi.org/10.1146/annurev-conmatphys-031016-025458

Keywords

surface states, Fermi arcs, magnetoresistance, chiral anomaly, anomalous Hall effect, spin Hall effect, Berry phase, monopole, transition-metal dichalcogenide, transition-metal pnictide, Heusler compound

Abstract

Topological insulators and topological semimetals are both new classes of quantum materials, which are characterized by surface states induced by the topology of the bulk band structure. Topological Dirac or Weyl semimetals show linear dispersion around nodes, termed the Dirac or Weyl points, as the three-dimensional analog of graphene. We review the basic concepts and compare these topological states of matter from the materials perspective with a special focus on Weyl semimetals. The TaAs family is the ideal materials class to introduce the signatures of Weyl points in a pedagogical way, from Fermi arcs to the chiral magnetotransport properties, followed by hunting for the type-II Weyl semimetals in WTe_2, $MoTe_2$, and related compounds. Many materials are members of big families, and topological properties can be tuned. As one example, we introduce the multifunctional topological materials, Heusler compounds, in which both topological insulators and magnetic Weyl semimetals can be found. Instead of a comprehensive review, this article is expected to serve as a helpful introduction and summary by taking a snapshot of the quickly expanding field.

1. INTRODUCTION

Insulators are known to be nonconducting because of a finite energy gap that separates the conduction and valence bands. Differences between insulators have been considered only quantitatively, such as in the band dispersion and the energy gap size. Over the past decade, we have learned that insulators can be further classified into different classes according to the topology of their band structures (1–4). For instance, the usual ordering conduction and valance bands of an ordinary insulator can be inverted by strong spin-orbital coupling (SOC), leading to a topological insulator (TI) (see **Figure 1*a***). The inverted bulk band structure topologically gives rise to metallic surface states. Therefore, a TI is characterized by gapless surface states inside the bulk energy gap. These surface states commonly exhibit a Dirac cone–type dispersion in which spin and momentum are locked-up and perpendicular to each other. TIs have been observed in many materials (5, 6), such as HgTe (7, 8) and Bi_2Se_3 (9, 10). Interestingly, similar to the surface states of TIs, topologicial surface states (TSSs) also exist on the surface of many exotic semimetals called Weyl semimetals (WSMs) (11–17). Identified by topological Fermi arcs on the surface and chiral magnetic effects in the bulk, WSMs have expanded the repertoire of exotic topological states.

In 1929, Hermann Weyl demonstrated the existence of a massless fermion in the Dirac equation (18), which was later called the Weyl fermion. In the standard model, all fermions are Dirac fermions, except possibly neutrinos that present chirality. However, neutrinos were later found to be massive and excluded from Weyl fermions. Weyl fermions have remained undiscovered until very recently in condensed matter systems (19–23). In solid-state band structures, Weyl fermions exist as low-energy excitations of the WSM, in which bands disperse linearly in three-dimensional (3D) momentum space through a node termed a Weyl point. The band structure of a WSM originates from the band inversion in proximity to a TI (see **Figure 1**) (24). The Berry curvature is a quantity that can characterize the topological entanglement between conduction and valence bands, which is equivalent to a magnetic field in the momentum space. The Berry curvature becomes singular at Weyl points that act as monopoles (12) in the momentum space with a fixed chirality: Such a Weyl point can be a source (+ chirality) or a sink (− chirality) of the Berry curvature. These Weyl points always appear in pairs (25, 26); otherwise, the Berry flux becomes divergent. The WSM requires the breaking of either the time-reversal symmetry (TRS) or the lattice inversion symmetry. When the TRS and inversion symmetry coexist, a pair of degenerate Weyl points may exist, leading to the related Dirac semimetal (DSM) phase (24, 27–29). In other words, a DSM can be regarded as two copies of WSMs. At the critical point during the transition from a TI to a normal insulator, the conduction and valence band touching points are the 3D Dirac points or Weyl points (24), and whether the critical points are Dirac or Weyl points depends on whether the inversion symmetry exists or not.

Although such gapless band touching has long been known, its corresponding topological nature has been appreciated only recently (11). Imagine a single pair of Weyl points in a WSM in which the TRS is naturally broken, as shown in **Figure 1*b***. The net Berry phase accumulated in the two-dimensional (2D) k plane between a pair of Weyl points induces a nonzero Chern number $C = 1$ with a quantized anomalous Hall effect (AHE), whereas the Berry phase is zero in other planes with $C = 0$. Therefore, the anomalous Hall conductivity of the 3D material corresponds to the quantized value (e^2/h) scaled by the separation of these two Weyl points (30–33). This is a pure topological effect from the band structure, because the bulk Fermi surface (FS) vanishes at the Weyl point. On the boundary, topological edge states exist at edges of 2D planes with $C = 1$ and disappear at edges of other planes in which the separation points between two types of planes are these Weyl points. Consequently, the FS, an energy contour crossing the Weyl points, exhibits an unclosed line that starts from one Weyl point and ends at the other with opposite chirality,

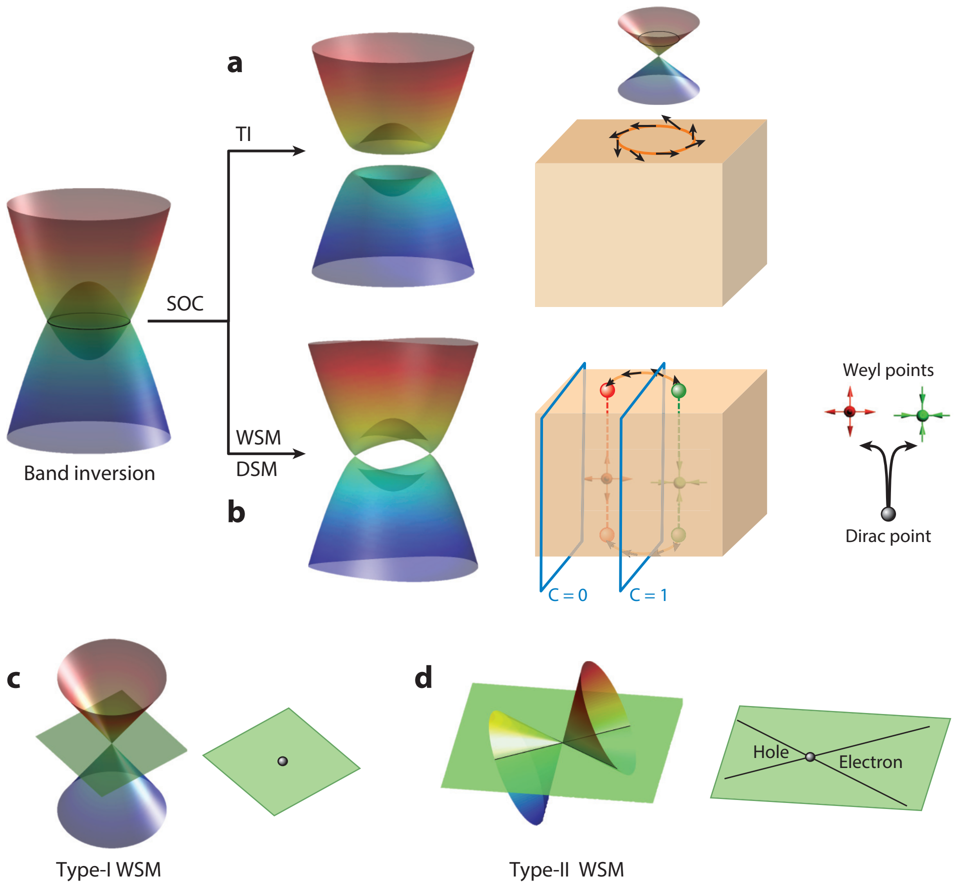

Figure 1

The topological insulator (TI) and Weyl semimetal (WSM) or Dirac semimetal (DSM). The topologies of a TI and that of a WSM/DSM originate from similar inverted band structures. (*a*) The spin-orbit coupling (SOC) opens a full gap after the band inversion in a TI, giving rise to metallic surface states on the surface. (*b*) In a WSM/DSM, the bulk bands are gapped by the SOC in the 3D momentum space except at some isolating linearly crossing points, namely Weyl points/Dirac points, as a 3D analog of graphene. Due to the topology of the bulk bands, topological surface states appear on the surface and form exotic Fermi arcs. In a DSM all bands are doubly degenerated, whereas in a WSM the degeneracy is lifted owing to the breaking of the inversion symmetry or time-reversal symmetry or both. (*c*) The type-I WSM. The Fermi surface (FS) shrinks to zero at the Weyl points when the Fermi energy is sufficiently close to the Weyl points. (*d*) The type-II WSM. Due to the strong tilting of the Weyl cone, the Weyl point acts as the touching point between electron and hole pockets in the FS.

which is called a Fermi arc. The Fermi arc is apparently different from the FS of a TI, an ordinary insulator, or a normal metal, which is commonly a closed loop. Therefore, the Fermi arc offers strong evidence for identifying a WSM by a surface-sensitive technique such as angle-resolved photoemission spectroscopy (ARPES). If TRS exists in a WSM, at least two pairs of Weyl points may exist, where TRS transforms one pair to the other by reversing the chirality. The Fermi arc still appears, as we discuss in this review. However, the AHE diminishes because the Berry phases contributed from two Weyl pairs cancel each other. Instead, an intrinsic spin Hall effect arises (34) that can be considered as the spin-dependent Berry phase and remains invariant under the TRS.

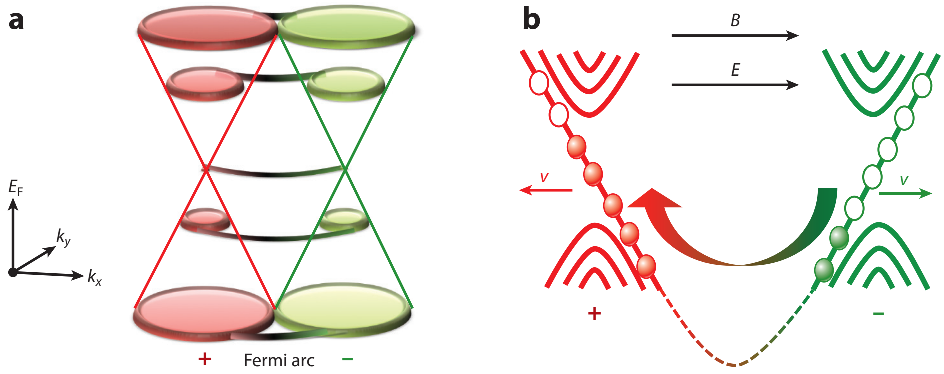

Figure 2

Schematics of Fermi arcs and the chiral anomaly effect. (*a*) Existence of Fermi arcs in the Fermi surface of the surface band structure. A pair of bulk Weyl cones exists as a pair of Fermi pockets at a Fermi energy $E_F \neq 0$ or as points at $E_F = 0$, where the pink (chartreuse) color represents the $+(-)$ chirality. A Fermi arc (*thick line*) appears on the top or bottom surface to tangentially connect such a pair of Fermi pockets. (*b*) The chiral anomaly can be simply understood with the zeroth Landau level of a Weyl semimetal in the quantum limit. The zeroth Landau levels from the + and − chiral Weyl cones exhibit opposite velocities due to different chirality. Applied electric field leads to an imbalance of electron densities in the left-hand and right-hand valleys, breaking the number conservation of electrons at a given chirality. This result, however, is not limited to the quantum limit and was recently proposed to induce an anomalous DC current that is quadratic in the field strength in the semiclassical limit.

An important consequence of the 3D Weyl band structure is that WSMs display the chiral anomaly effect (see **Figure 2**). In high-energy physics, the particle number of Weyl fermions for a given chirality is not conserved quantum mechanically in the presence of nonorthogonal magnetic (**B**) and electric (**E**) fields (i.e., $\mathbf{E} \cdot \mathbf{B}$ is nonzero), inducing a phenomenon known as the Adler–Bell–Jackiw anomaly or chiral anomaly (35, 36). In WSMs, the chiral anomaly is predicted to lead to a negative magnetoresistance (MR) owing to the chiral zero modes of the Landau levels of the 3D Weyl cones and the suppressed backscattering of electrons of opposite chirality (37, 38). The negative MR is expected to exhibit the largest amplitude when $\mathbf{B} \parallel \mathbf{E}$, because the $\mathbf{B} \perp \mathbf{E}$ component contributes a positive MR due to the Lorentz force. In addition to the negative MR, the chiral anomaly is also predicted to induce exotic nonlocal transport and optical properties (39–41).

Many material candidates have been predicted as WSMs, e.g., the pyrochlore iridates $Y_2Ir_2O_7$ (11), $HgCr_2Se_4$ (30), and $Hg_{1-x-y}Cd_xMn_yTe$ (42). However, these candidates have not been experimentally realized thus far. In early 2015, four WSM materials—TaAs, TaP, NbAs, and NbP—were discovered through calculations (19, 20) and the observation of Fermi arcs using ARPES (21–23), realizing Weyl fermions for the first time [also in photonic crystals (43)]. Meanwhile, many efforts have been devoted to their magnetotransport properties (44–47). These WSM compounds preserve TRS but break crystal inversion. In addition, the DSMs were found to exist in Na_3Bi and Cd_3As_2 by ARPES (48–51).

WSMs can be classified into type I, which respects Lorentz symmetry, and type II, which does not (see **Figure 1**) (52). The TaAs family of WSMs exhibits ideal Weyl cones in the bulk band structure and belongs to the type-I class, i.e., the FS shrinks to a point at the Weyl point. More recently, type-II WSMs have been proposed to exist in the layered transition-metal dichalcogenides WTe_2 (52) and its sister compound $MoTe_2$(53). Here, the Weyl cone exhibits strong tilting so that the Weyl point is the contact point between an electron pocket and a hole pocket in the FS. Type-II WSMs are expected to show very different properties from type-I WSMs, such as anisotropic chiral anomaly depending on the current direction and a novel AHE (52). In addition, the layered nature of these compounds can facilitate the fabrication of devices, making them an ideal platform for the realization of novel WSM applications.

In this review, we give an overview of recent progress in topological states of matter from the viewpoint of materials. We start from the TaAs family of WSMs by introducing their surface states and chiral magnetotransport properties. We further follow the recent search for type-II WSMs in $MoTe_2$ and related compounds. Then, we introduce the multifunctional topological materials termed Heusler compounds, in which both TIs and TRS-breaking WSMs can be found.

2. WEYL SEMIMETALS: THE TaAs FAMILY

2.1. Bulk and Surface States

We first use the TaAs-type compounds to demonstrate the properties of WSMs. We answer a simple but essential question in a pedagogical manner: How can we identify a WSM in both theory and experiment?

2.1.1. Weyl points as the band-crossing points. According to the definition, the conduction and valence bands touch at the Weyl points in the bulk band structure, which is usually obtained from state-of-the-art ab initio calculations. Therefore, the first step is to address these gapless points in the 3D Brillouin zone (BZ). Sometimes, it can be challenging because Weyl points usually stay away from high-symmetry lines or planes and their total numbers are not easy to identify. Fortunately, the band structure without including SOC can provide insightful hints for solving this problem. Take TaP as an example (see **Figure 3**). TaP crystallizes into a noncentrosymmetric tetragonal lattice (space group $I4_1md$, No. 109) that contains two mirror planes, M_x and M_y. One can find band crossing at some high-symmetry lines in the band structure when SOC is turned off. These gapless points form nodal rings in the mirror planes in the BZ. When SOC is switched on, the band structure exhibits spin splitting due to the lack of inversion symmetry. Consequently, the nodal lines are all gapped. However, band-touching points exist near the original nodal rings but away from the mirror planes. A single nodal ring evolves into three pairs of gapless points that can be classified into two groups, one pair in the $k_z = 0$ plane (labelled W1) and two pairs in the $k_z \approx \pm\pi/c$ planes, where c is the lattice parameter along the z axis. In total, there are twelve pairs of Weyl points, considering four nodal rings inside two mirror planes in the first BZ. Along a line that connects a pair of Weyl points, one can find that the conduction and valence bands indeed cross each other linearly through Weyl points (**Figure 3*c***). We point out that Weyl points W1 and W2 appear at slightly different energies in the band structure. Experimentally, the linear dispersions near two types of Weyl points have been visualized using soft X-ray ARPES, which is sensitive to the bulk states (21, 23, 56).

2.1.2. Weyl points as monopoles. The topology of Weyl points can be verified through the Berry curvature. The Berry curvature $\mathbf{\Omega}(\mathbf{k})$ characterizes the wave-function entanglement between the conduction and valence bands and is considered as an effective magnetic field (a pseudo-vector) in the k-space, which can be obtained based on the Bloch wave functions from band-structure calculations (57, and references therein). The Weyl point behaves as a monopole, i.e., a source or sink of this field. The corresponding magnetic charge, i.e., chirality χ, can be found as an integral over the the FS enclosing the Weyl point, $\chi = \frac{1}{2\pi}\oint_{\mathrm{FS}} \mathbf{\Omega}(\mathbf{k}) \cdot d\mathbf{S}(\mathbf{k})$. In this manner, the monopole feature of all Weyl points can be identified for TaP. Although many Weyl points exist in the BZ, we can easily organize them according to their symmetry. Regarding two mirror planes M_x

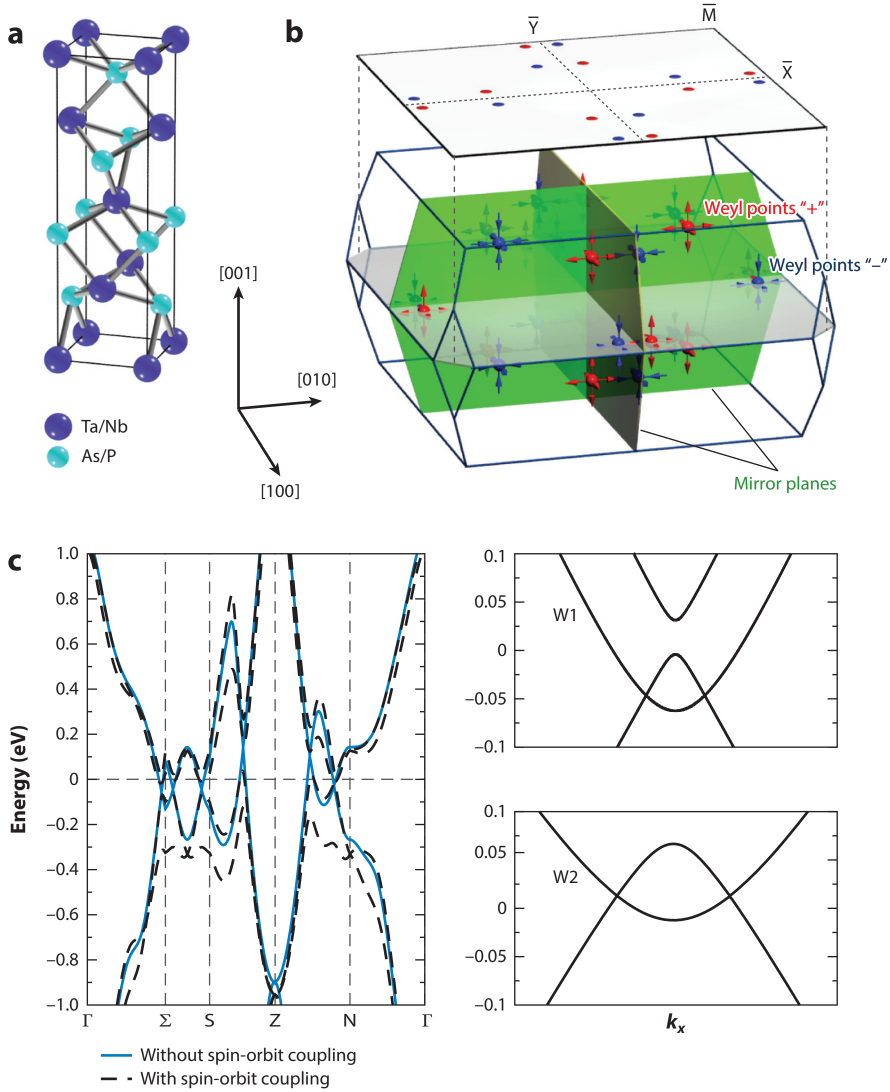

Figure 3

Crystal structure and bulk band structure. (*a*) The noncentrosymmetric crystal lattice of TaAs-family compounds. Adapted from Reference 54 with permission. (*b*) The first Brillouin zone with twelve pairs of Weyl points. The red and blue spheres represent the Weyl points with "+" and "−" chirality, respectively. The arrows that surround a Weyl point stand for the monopole-like distribution of the Berry curvature. Adapted from Reference 54 with permission. (*c*) The bulk band structure along some high-symmetry lines. The solid blue lines and black dashed lines correspond to the presence and absence of spin-orbit coupling, respectively. The energy dispersions crossing a pair of W1 and W2 Weyl points are shown in the right panels. The Fermi energy is set to zero. Adapted from Reference 55 with permission.

and M_y that reverse the chirality, one Weyl point at the position (k_x, k_y, k_z) with, for instance, chirality $\chi = 1$ has three partners: one each at $(-k_x, k_y, k_z)$ and $(k_x, -k_y, k_z)$ with $\chi = -1$ and one at $(-k_x, -k_y, k_z)$ with $\chi = 1$. Considering the TRS that preserves the chirality, the above four Weyl points have four time-reversal partners at $(\pm k_y, \pm k_x, \pm k_z)$. Further, these eight Weyl points at $(\pm k_x, \pm k_y, \pm k_z)$ find another eight partners at $(\pm k_y, \pm k_x, \pm k_z)$ that are connected by the C_4 rotational symmetry that also maintains the chirality. Therefore, there are eight W1-type Weyl points since $k_z = 0$ and sixteen W2-type Weyl points since $k_z \neq 0$.

2.1.3. Fermi arcs on the surface. A significant consequence of the monopole feature of Weyl points is the existence of Fermi arcs in the FS of the surface states. Consider a simple WSM in which only a pair of Weyl points exists with TRS breaking and slices not containing the Weyl points in the BZ are gapped as 2D insulators. If the slices lie between two Weyl points, the net Berry flux accumulated across the slices leads to Chern insulators with a nonzero Chern number (C), which carry chiral edge states. If the slices stay far away from the two Weyl points, they are trivial 2D insulators. Thus, the chiral edge states exist only between these two Weyl points and assemble a TSS. When the Fermi energy crosses the Weyl points, a Fermi arc exists to connect the surface projections of two Weyl points (see **Figure 2**). The Fermi arcs from the top and bottom surfaces are related through the bulk Weyl points, which can generate fascinating transport and optical phenomena (40, 41, 58). The 3D band structures are shown in **Figure 2**. When the Fermi energy is away from the Weyl points, the Fermi arc tangentially connects two bulk Weyl pockets. We point out that the Fermi arcs may appear even when two Weyl pockets merge. However, these argument based on the Chern number cannot be applied for TaP because of the existence of TRS, which constrains the Chern number to be zero. Instead, the same topological Z_2 index as that of a TI can be defined to identify the Fermi arcs (19). The mirror plane, for example M_x in the BZ that lies between six pairs of Weyl points, is a gapped 2D TI exhibiting a nontrivial Z_2 index. Consequently, helical edge states exist, which form Fermi arcs in the surface band structure as well.

The existence of Fermi arcs is topologically protected by the Weyl points in the underlying bulk. However, the shape and energy dispersion of Fermi arcs is sensitive to the surface. Indeed, it is found that the surfaces terminated by cations (Ta, Nb) and anions (As, P) present very different FSs in ab initio simulations (55). In general, anion-terminated surfaces were usually reported for the as-cleaved surface in ARPES for TaAs (21–23), TaP (54), NbAs (59) and NbP (54, 60), while anion-terminated surfaces were also observed for TaP (61) and NbP (62). The typical FS of the As- or P-terminated surface is shown in **Figure 4**; it is composed of spoon-like and bowtie-like parts. Two pieces of Fermi arcs appear at the head of the spoon-like region, connecting the projections of W2-type Weyl points. These two arcs exhibit opposite spin texture (23, 55, 63, 64). The separation of W2 Weyl points with opposite chirality and the length of corresponding Fermi arcs are proportional to the strength of SOC, i.e., decreasing in the order of TaAs, TaP, NbAs, and NbP (54, 55). The bowtie-like part is due to the p-orbital dangling bond states of As or P. As demonstrated by calculations, these dangling bonds can be passivated, for instance, by the guest atom deposition, resulting in a Lifshitz transition of FS that is purely composed of the Fermi arcs (55). Additionally, the Fermi arcs can also be visualized in scanning tunneling spectroscopy (65, 66), where the topology of the FS and its spin texture are essential to understand the quasiparticle interference on the surface of WSMs (67).

2.2. Chiral Magnetotransport

The magnetotransport properties have been quickly and widely studied for WSM materials. The linear dispersion and nontrivial Berry phases in the band structure allow the detection of chiral

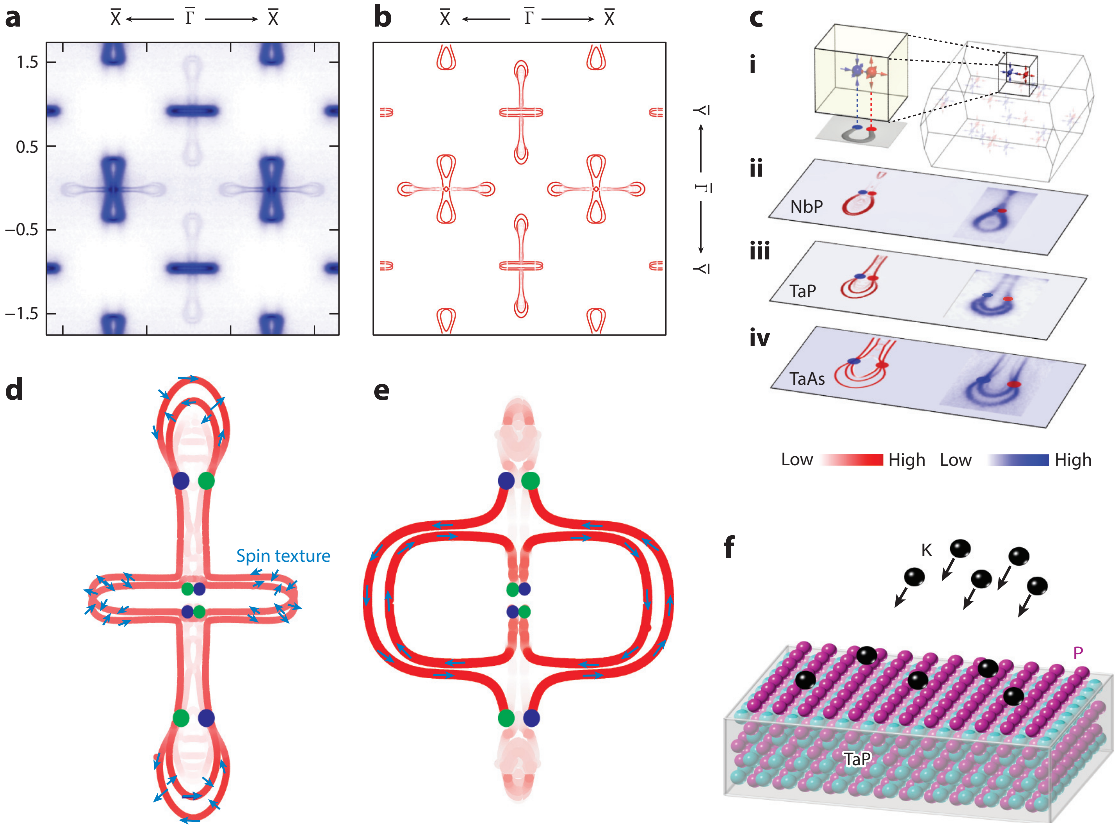

Figure 4

Fermi arcs from angle-resolved photoemission spectroscopy (ARPES) and theoretical calculations. The Fermi surface (FS) of TaP by (*a*) ARPES and (*b*) calculations agree very well. (*c*) Evolution of the band structures for NbP, TaP, and TaAs, in which spin-orbit coupling increases in order. (*c*, *i*) Schematic plot (*gray curves*) connecting them. (*c*, *ii–iv*) Comparison of the (*left*) calculated to the (*right*) ARPES Fermi arcs for different compounds. Red/blue dots denote the Weyl points of opposite chirality. Panels *a*, *b*, and *c* adapted from Reference 54 with permission. (*d*) The FS around the Ȳ point. The spoon-head part corresponds to the Fermi arcs. The bowtie-like middle part is due to trivial surface states. Blue arrows indicate the spin texture. Adapted from Reference 55 with permission. (*e*) Calculated new FS after a Lifshitz transition, which is formed purely by long Fermi arcs. Adapted from Reference 55 with permission. (*f*) The illustration of the Lifshitz transition induced by depositing potassium atoms on the TaP surface.

magnetotransport phenomena, large MR, and high mobility as well. Strong quantum oscillations also assist the reconstruction of the Fermi surface information, further validating and revealing the physics behind.

2.2.1. Chiral anomaly and fermiology. The discovery of WSM materials triggered an experimental search for the exotic quantum phenomenon known as the chiral anomaly in condensed matter physics. Recently, a negative longitudinal MR, the resistivity change under magnetic field $[\Delta\rho(B)/\rho(0)]$ and $\mathbf{B}||\mathbf{I}$, has been reported in two types of WSMs: WSMs induced by TRS breaking, i.e., DSMs in an applied magnetic field, for example, $Bi_{1-x}Sb_x$ ($x \approx 3\%$) (68), $ZrTe_5$ (69), Na_3Bi (70), and Cd_3As_2 (71); and the noninversion-symmetric WSMs TaAs (44, 45), TaP (47), and NbP (72). All these systems are semimetals with a very high mobility as in classical semimetals such as bismuth and graphite. The chiral anomaly is believed to induce the negative longitudinal

MR (37, 38). However, the negative longitudinal MR does not solely originate from the chiral anomaly effect. For example, it can be induced by the inhomogeneous current distribution in the device (47, 73), a generic 3D metal in the quantum limit (74), or other effects without necessarily evolving Weyl points (75–77). Therefore, a clear verification of the existence of Weyl points in the FS topology is crucial to interpret the MR experiments.

In the TaAs family of WSMs, two types of Weyl points, W1 and W2, exist at different momentum positions and energies. In the FS, the Weyl electrons generally coexist with topologically trivial normal electrons. In principle, small changes of the Fermi energy (E_F), as induced by doping or defects, can significantly change the FS topology owing to the low intrinsic charge-carrier density in semimetals. Even in the ideal case of completely stoichiometric and compensated crystals, the Fermi energy does not necessarily cross the Weyl points. Therefore, a precise knowledge of E_F and the resulting FS topology is required when linking the negative MR to the chiral-magnetic effect. Although ARPES studies have shown the existence of Fermi-arc surface states and linear band crossings in the bulk band structure of all four materials, its energy resolution (>15 meV) is insufficient to confirm the presence or absence of Weyl fermions at the Fermi level. In contrast, quantum-oscillation measurements have the advantage of meV-order resolution of the Fermi level. Quantum oscillations originating from different types of FS pockets were found in magnetization, magnetic torque, and MR measurements performed in magnetic fields at low temperature. These oscillations are periodic with respect to $1/B$. Their frequency (F) is proportional to the corresponding extremal FS cross section (A) that is perpendicular to $\mathbf{B}$ following the Onsager relation $F = (\Phi_0/2\pi^2)A$, where $\Phi_0 = h/2e$ is the magnetic flux quantum and h is the Planck constant. To reconstruct the shape of the FS, the full angular dependence of the quantum-oscillation frequencies was compared to band-structure calculations (47, 78). The exact position of E_F was determined by matching the calculated frequencies and their angular dependence to the experimental ones.

The 3D FSs of TaAs (78), TaP (47), and NbP (79) have very recently been reconstructed by combining sensitive angle-dependent Shubnikov–de Haas and de Haas–van Alphen oscillations with ab initio band-structure calculations, showing excellent agreement between theory and experiment. In these semimetals, electron and hole pockets coexist near the nodal ring positions in the FS, as shown in **Figure 4**. For TaAs, E_F crosses the upper parts of both W1 and W2 Weyl cones, leading to independent W1 and W2 electron pockets. This type of FS can suppress the scattering between a pair of Weyl valleys with opposite chirality, supporting the existence of the chiral anomaly effect. However, the results for TaP and NbP are not found to be the same. E_F is located far above the W1 Weyl points and slightly below the W2 Weyl points. Consequently, W1 and W2 Weyl points are swallowed inside large electron and hole pockets, respectively. The disappearance of the individual Weyl pocket, which includes a single Weyl point, quenches the chiral anomaly effect. Instead, the negative MR observed in TaP was further explained as a field-induced current redistribution (47). With the aim of realizing chiral anomaly in TaP and NbP, electron doping was suggested to shift the Fermi energy in the close vicinity of the W2 Weyl points (47, 79). In addition, the topology of the FS was found to be robust under external pressure up to ~2–3 GPa (80, 81). In NbP the W2 Weyl points were found to move close to the Fermi energy by 3 meV corresponding to a pressure of ~3 GPa (81).

2.2.2. Large positive magnetoresistance and high mobility. WSMs and DSMs usually exhibit very high mobilities that can probably be attributed to the chiral and massless feature of Weyl or Dirac fermions and the high Fermi velocity, as observed in transport experiments with materials such as Cd_3As_2 (82, 83) and NbP (46). Generally, semimetals are new platforms realizing a huge transverse MR ($\mathbf{B}\perp\mathbf{I}$), an effect that has been pursued intensively in emerging materials in recent years because of its significant potential for application in state-of-the-art information technologies (84). Electrical transport in a semimetal usually consists of two types of carriers (electrons and holes), leading to large MR when a magnetic field is applied with an electron–hole resonance (85). In a simple Hall effect setup, the transverse current carried by a particular type of carrier may be nonzero, although no net transverse current flows when the currents carried by the electrons and holes compensate for each other. These nonzero transverse currents will experience a Lorentz force caused by the magnetic field in the inverse-longitudinal direction. Such a backflow of carriers eventually increases the apparent longitudinal resistance, resulting in a dramatic MR that is much stronger than that in normal metals and semiconductors. Thus, high-purity samples are crucial for realizing a balance between electrons and holes and a high carrier mobility (μ), both of which will enhance the positive MR.

In the TaAs family of WSMs, NbP (46) was first reported to exhibit an extremely large positive MR of 850,000% at 1.85 K (250% at room temperature) in a magnetic field of up to 9 T, which increases linearly up to 60 T without any signs of saturation (see **Figure 5*e***). Ultrahigh carrier mobility accompanied by strong Shubnikov–de Haas oscillations was also observed. A perfect electron-hole compensation was identified on the FS (79), explaining the large MR observed. Similar behaviors were also observed in other compounds of this family (44, 45, 72, 86–88). Therefore, this family of WSMs presents profound examples of materials that combine topological and conventional electronic phases with intriguing physical properties resulting from their interplay.

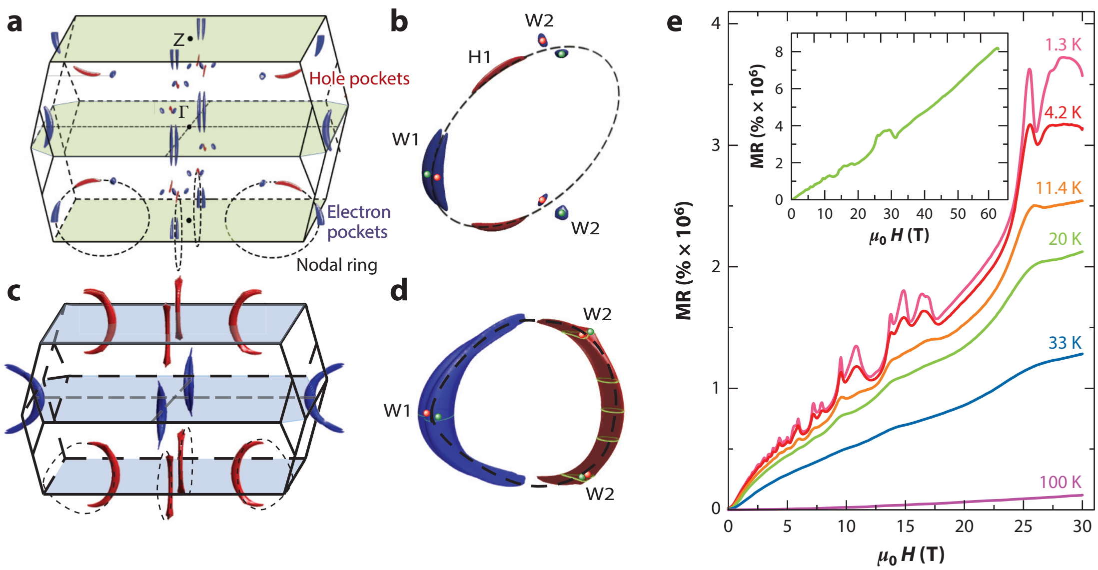

Figure 5

Bulk Fermi surfaces (FSs) constructed by quantum oscillations and calculations. (*a*,*b*) TaAs FS. Blue and red FSs correspond to electron and hole pockets, respectively. The dashed loop represents the nodal ring. The positions of Weyl points are indicated by red/green points. Each Weyl point (both W1 and W2 types) is independently included inside a single electron pocket, which is active for the chiral anomaly. Panels *a* and *b* adapted from Reference 78 with permission. (*c*,*d*) TaP Fermi surface. All W1 and W2 Weyl points are included inside large electron and hole pockets, respectively. Panels *c* and *d* adapted from Reference 47 with permission. (*e*) Large transverse magnetoresistance (MR) with Shubnikov–de Hass oscillations measured on NbP. Adapted from Reference 46 with permission.

3. WEYL SEMIMETALS: TYPE II

3.1. Bulk and Surface States

The layered transition-metal dichalcogenide WTe_2 was the first theoretically predicted candidate for the type-II WSM (52). Corresponding Fermi arcs were demonstrated between a pair of Weyl points separated by ~0.7% of the BZ width and located approximately 50 meV above E_F, which seems to be challenging for detection using ARPES. Soon, a similar compound, $MoTe_2$ (53), was proposed to be an optimized version of WTe_2 in which the Fermi arcs are six times longer than those of WTe_2 and Weyl points are located merely 6 meV above E_F. Additionally, $W_xMo_{1-x}Te_2$ was also proposed to be a WSM as an alloyed version of the above two compounds (89). WTe_2 and $MoTe_2$ crystallize into the same type of orthorhombic lattice without inversion symmetry and show very similar band structures. In the following, we take $MoTe_2$ as an example.

There are four pairs of Weyl points in the $k_z = 0$ plane in the BZ of $MoTe_2$ (53), as shown in **Figure 6*b***. In the FS, these Weyl points indeed behave as the contact points between the electron and hole pockets. We point out that the band structure is quite sensitive to external strain. Density–functional theory calculations based on slightly shorter lattice parameters revealed that only two pairs of Weyl points exist, whereas the other two pairs were annihilated by merging at the $\Gamma - X$ line (53, 90). When these four or two pairs of Weyl points are projected to the surface, Fermi arcs appear to connect each pair of Weyl points with another pair that are of opposite chirality. Owing to the uncertainty of the sample and experimental conditions, there are three possible

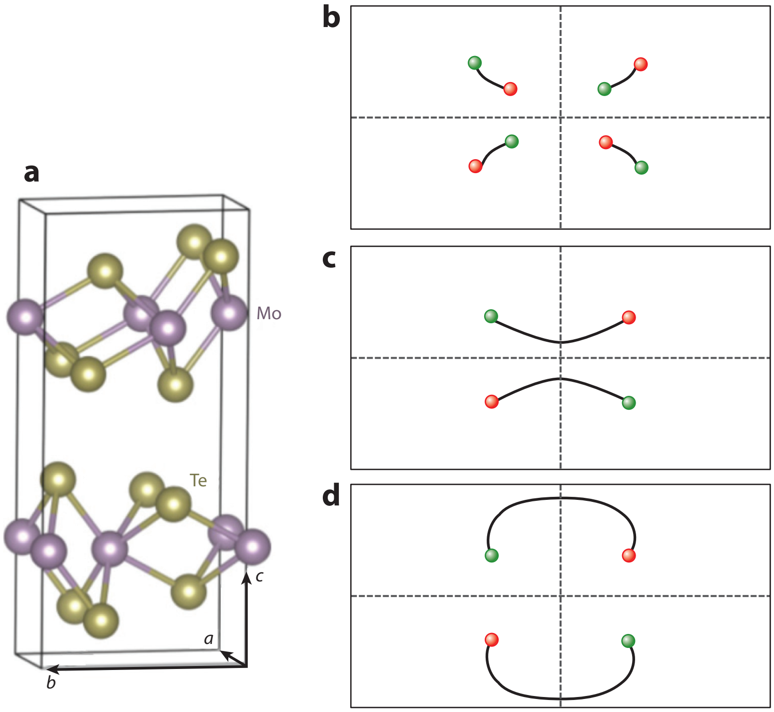

Figure 6

Crystal structure and schematics of Fermi arcs for $MoTe_2$. (*a*) The layered crystal structure (T_d phase) with inversion symmetry breaking. (*b–d*) Three possible scenarios of the Fermi arcs and Weyl points on the surface.

scenarios for the connectivity of these Fermi arcs, as demonstrated in **Figure 6**. The theoretical predictions led to immediate and tremendous experimental activities to verify the type-II WSMs in both $MoTe_2$ (91–94) and WTe_2 (95–97). However, these works reported different pictures of Fermi arcs including the above three scenarios and even different interpretations, which deserve further investigation before the convergence of conclusions.

3.2. Magnetoresistance and Superconductivity

The type-I WSM exhibits chiral anomaly for all directions of the chiral anomaly. However, the type-II WSM is argued to show a chiral anomaly only when the magnetic direction is normal to a momentum plane that shows a point-like FS by intersecting the Weyl point (52); otherwise, the chiral anomaly effect disappears because the Landau-level spectrum is gapped without chiral zero modes. Longitudinal MR measurements are still called for to address the chiral anomaly in WTe_2, $MoTe_2$, and related systems.

It is not surprising that WTe_2 and $MoTe_2$ show large transverse MR. Before the discovery of type-II WSMs, WTe_2 was already reported for the extremely large MR that increases nearly quadratically with the field (98) for which the topological origin was further proposed more recently (99). A large transverse MR was also observed for $MoTe_2$ (100, 101). Interestingly, $MoTe_2$ exhibits superconductivity with a transition temperature of $T_c = 0.10$ K under ambient conditions (101). Under external pressure, both $MoTe_2$ and WTe_2 are superconducting with a dome-shaped superconductivity phase diagram in which the highest transition temperatures are $T_c = 8.2$ K at 11.7 GPa (101) and $T_c \approx 7$ K at 16.8 GPa (102, 103), respectively.

4. MULTIFUNCTIONAL HEUSLER MATERIALS

4.1. Heusler Topological Insulators

The Heusler compounds with their great diversity (more than 1,500 members) give us the opportunity to search for optimized parameters (SOC strength, gap size, etc.) across different compounds, which is critical not only for realizing the topological order and investigating the topological phase transitions but also for designing realistic applications (104). In addition, among the wealth of Heusler compounds, many (especially those containing rare earth elements with strongly correlated f electrons) exhibit rich, interesting ground-state properties (105), such as magnetism (106), unconventional superconductivity (107–111), and heavy fermion behavior (112). The interplay between these properties and the topological order makes Heusler compounds ideal platforms for the realization of novel topological effects [e.g., exotic particles exhibiting the image monopole effect and axions (1)], new topological phases [e.g., topological superconductors (113)], and broad applications (see Reference 104 for a review).

Rare earth Heusler compounds LnPtBi (Ln = Y, La, and Lu) represent a recently proposed model system that can possess topological orders with nontrivial TSSs and large band inversion (114–116). These compounds have a noncentrosymmetric lattice (space group $F\bar{4}3m$, No. 216). The structure of LnPtBi consists of three interpenetrating *fcc* lattices; along the [111] direction, the structure can be described as a metallic multilayer formed from successive atomic layers of the rare earth elements platinum and bismuth. A band inversion between the Γ_8 and Γ_6 bands results in a gapless semimetal with degenerate Γ_8 bands at the Fermi energy. Because it exhibits an inverted band structure similar to that of HgTe (7), LnPtBi is also a TI.

Despite the great interest and intensive research efforts in both theoretical (114–116) and experimental (117–119) investigations, the topological nature of Heusler TIs has remained elusive until recently (120, 121). The Dirac-type surface states have been resolved by performing comprehensive ARPES measurements and ab initio calculations in the Heusler compounds LuPtBi, YPtBi (120), and LuPtSb (121). Remarkably, in contrast to many TIs that have TSSs inside their bulk gap, the TSSs in LnPtBi show their unusual robustness by lying well below the E_F and strongly overlapping with the bulk valence bands [similar to those in HgTe (122–124)]. In addition to the TSSs, numerous metallic surface states were observed to cross the E_F with large Rashba splitting, which not only makes them promising compounds for spintronic application but also provides the possibility to mediate topologically nontrivial superconductivity in the superconducting phase of these compounds.

4.2. Heusler Magnetic Weyl Semimetals

The combination of band inversion and magnetism in the same Heusler compound provides a way to design the magnetic WSM. When substituting Ln with most of the lanthanides, the f electrons give rise to magnetism. For example, when Ln = Gd or Nd, GdPtBi and NdPtBi exhibit magnetism arising from their 4f electrons, but the Γ_8–Γ_6 band inversion is preserved. GdPtBi (126, 127) as well as NdPtBi (128) are antiferromagnetic (AFM) at low temperatures below their corresponding transition temperatures, $T_N = 9.0$ K and 2.1 K, respectively. The magnetic structures of these compounds are different: GdPtBi is a type-II antiferromagnet, whereas the magnetic structure of NdPtBi is of type I, indicating that the concrete magnetic ordering below the Néel temperature does not influence the Weyl physics, as we discuss below. Additionally, one should be aware that the size, anisotropy moments, and degeneracy are distinguished for neodymium and gadolinium.

Electronic structure calculations were performed on GdPtBi and YPtBi, as exemplary magnetic and nonmagnetic compounds, respectively, to understand the transition from a TI to a magnetic WSM (125). A schematic diagram of their energy bands is shown in **Figure 7**. In GdPtBi, the Gd-4f bands are well localized at energies below the Fermi energy, but we find large exchange-derived spin-splitting of the Γ_8 and Γ_6 bands in GdPtBi when there is a net magnetization induced by an external magnetic field, which is absent in YPtBi. It should be noted that the exchange splitting can be as large as 0.5 eV. In the presence of an external magnetic field, the magnetization of the Gd moments can be aligned in modest fields, forcing GdPtBi into a ferromagnetic (FM) state. This leads to a pair of Weyl points where the valence and conduction bands touch each other. The orientation of the magnetic moments sensitively affects the FS and changes the positions and numbers of the Weyl points. For instance, four pairs of Weyl points exist slightly below the Fermi energy when the magnetic moments are along the [111] direction (**Figure 1*b***) while six pairs of Weyl points appear at different positions in the BZ when the moments are oriented along the [001] direction (125).

Recently, experimental studies have shown that GdPtBi and NdPtBi become WSMs when the exchange splitting of the Γ_8 and Γ_6 bands is sufficiently large to establish the Weyl points (125, 129). This is established for applied fields only of the order of tesla. It is clear that this is hardly possible from Zeeman splitting in the band structure; rather, the external field results in a significant alignment of the magnetization of the AFM structure, resulting in a large exchange field (125). Although the magnitude of this exchange field will increase up to the saturation field (~25 T at $T = 1.4$ K), it is clear that once the exchange field is sufficiently large to induce the Weyl modes, the interesting quantum phenomena of Weyl physics can emerge. Here, GdPtBi and NdPtBi show two strong signatures of the chiral anomaly: a large nonsaturated negative quadratic MR for fields up to 60 T when a magnetic field was applied parallel to the current direction and an unusual intrinsic AHE. These signatures, however, are absent in YPtBi, indicating that the f electrons of Gd and Nd must play an essential role in generating the Weyl points. Therefore,

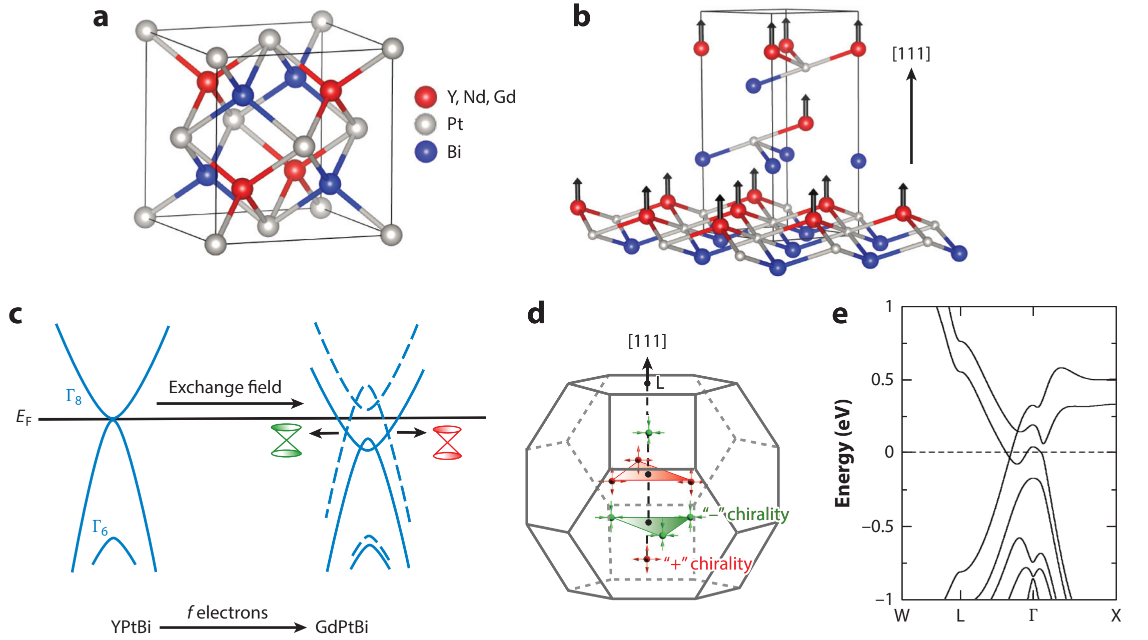

Figure 7

Crystal and band structures of Heusler Weyl semimetals. (*a*) Cubic unit cell of LnPtBi (Ln = Y, Gd, or Nd). (*b*) View of the structure showing Ln-Pt-Bi–type layers stacked along the [111] axis. The magnetic moments of the Ln atoms are shown as arrows corresponding to the fully saturated FM state. (*c*) Schematic comparison of the band structures of YPtBi and GdPtBi. The exchange field from the Gd moments lifts the spin degeneracy of the Γ_8 and Γ_6 bands and induces Weyl points that are slightly below the Fermi energy: The green and red hourglasses represent Weyl cones with opposite chirality. (*d*) The distribution of Weyl points in the first Brillouin zone when the Gd magnetic moments are fully saturated along [111] (as shown in panel *b*). Green and red spheres represent − and + chirality, respectively, where the arrows are the Berry curvature vectors. (*e*) The calculated band structure of GdPtBi (corresponding to panel *c*). Adapted from Reference 125 with permission.

it is speculated that all magnetic rare earth Heusler compounds such as LnPtBi and LnAuSn (Ln = Ce-Sm, Gd-Tm) will show related properties.

The magnetic field, its direction and strength, allows for the tuning of the position and the number of Weyl points in the magnetic Heusler compound. As another proof of the tunability of the band structure, the Seebeck effect is observed to depend strongly on the magnetic field in GdPtBi (129). The Seebeck effect is a voltage generated by a gradient of temperature and intimately determined by the band structure. Therefore, a magnetic field that tailors the band structure sensitively alters the Seebeck effect.

Many other magnetic and nonmagnetic Heusler compounds have recently been reported to be WSM candidates, such as the Co-based Heusler materials XCo_2Z (X = V, Zr, Nb, Ti, Hf; Z = Si, Ge, Sn) (130) and strained Heulser TI materials (131). Weak TIs (132) and nonsymmorphic symmetry-protected topological states (133) have been reported in the KHgSb honeycomb Heulser materials. Nonsymmorphic symmetry-protected DSMs have also been reported in the AFM Heusler material CuMnAs (134). The chiral AFM Heusler compounds Mn_3X (X = Sn, Ge) that exhibit a strong AHE at room temperature (135, 136) were also predicted to be AFM WSMs (137). Additionally, several other Heusler-like ternary compounds such as ZrSiS (138) and LaAlGe (139) were also found to be topological semimetals. Thus, we expect that more WSMs and DSMs will be discovered in the multifunctional and abundant Heusler family and similar compounds.

5. SUMMARY AND OUTLOOK

Thus far, several materials have been discovered as WSMs in which Weyl points, Fermi arcs, chiral-anomaly-induced negative MR, or the AHE has been demonstrated. However, considerable trivial carrier pockets still coexist with the Weyl pockets in the FS, which complicates the interpretation of the experimental results. Thus, pure WSM materials are still strongly needed, and only linear Weyl bands appear with the Weyl points located sufficiently close to the Fermi energy. An ideal WSM is expected to exhibit only a single pair of Weyl points at the Fermi energy, within which two Weyl points are well separated in momentum space. Current materials are usually in the single-crystal form, whereas high-quality thin films will be favored for building devices.

The exotic properties of WSMs show great potential for applications. By exploiting the high mobility and large MR, WSMs can be employed in high-speed electronics and spintronics. We stress that WSMs may exhibit the strong spin Hall effect and related phenomena (34) owing to the large Berry curvature and SOC, which is expected to be important for spin Hall effect devices that can efficiently convert charge current to spin current (140). Finally, one vision for TIs and WSMs is to utilize their robust surface states for surface-related chemical processes such as catalysis (141, 142). A preliminary theoretical attempt was made to use the surface states of a TI to enhance the activity of traditional catalysts (143, 144) and even reveal TSSs on traditional catalysts such as gold and platinum (145). The existence of WSM materials has enriched the topological systems that can be considered for the potential design of topological catalysts.

DISCLOSURE STATEMENT

The authors are not aware of any affiliations, memberships, funding, or financial holdings that might be perceived as affecting the objectivity of this review.

ACKNOWLEDGMENTS

We are grateful for Yan Sun, Shu-Chun Wu, Chandra Shekhar, Arnoald Frank, Elena Hassinger, Adolfo G. Grushin, Jens H. Bardarson, Marcus Schmidt, Michael Nicklas, Ajaya K. Nayak, Uli Zeitler, Jochen Wosnitza, Zhongkai Liu, Yulin Chen, and S.S.P. Parkin, for their close collaboration and for their important contributions reviewed in this paper. We acknowledge financial support from the Max Planck Society and the European Research Council Advanced Grant (291472 "Idea Heusler").

LITERATURE CITED

1. Qi XL, Zhang SC. 2011. *Rev. Mod. Phys.* 83:1057
2. Hasan MZ, Kane CL. 2010. *Rev. Mod. Phys.* 82:3045–67
3. Maciejko J, Hughes TL, Zhang SC. 2011. *Annu. Rev. Condens. Matter Phys.* 2:31–53
4. Hasan MZ, Moore JE. 2011. *Annu. Rev. Condens. Matter Phys.* 2:55–78
5. Yan B, Zhang SC. 2012. *Rep. Prog. Phys.* 75:096501
6. Ando Y. 2013. *J. Phys. Soc. Jpn.* 82:102001
7. Bernevig BA, Hughes TL, Zhang SC. 2006. *Science* 314:1757
8. König M, Wiedmann S, Brüne C, Roth A, Buhmann H, et al. 2007. *Science* 318:766–70
9. Zhang H, Liu CX, Qi XL, Dai X, Fang Z, Zhang SC. 2009. *Nat. Phys.* 5:438–42

10. Xia Y, Qian D, Hsieh D, Wray L, Pal A, et al. 2009. *Nat. Phys.* 5:398–402
11. Wan XG, Turner AM, Vishwanath A, Savrasov SY. 2011. *Phys. Rev. B* 83:205101
12. Volovik GE. 2003. *The Universe in a Helium Droplet*. Oxford: Clarendon Press
13. Balents L. 2011. *Physics* 4:36
14. Burkov AA, Hook MD, Balents L. 2011. *Phys. Rev. B* 84:235126
15. Hosur P, Qi XL. 2013. *C. R. Phys.* 14:857–70
16. Vafek O, Vishwanath A. 2014. *Annu. Rev. Condens. Matter Phys.* 5:83–112
17. Witczak-Krempa W, Chen G, Kim YB, Balents L. 2014. *Annu. Rev. Condens. Matter Phys.* 5:57–82
18. Weyl H. 1929. *PNAS* 15:323–34
19. Weng H, Fang C, Fang Z, Bernevig BA, Dai X. 2015. *Phys. Rev. X* 5:011029
20. Huang SM, Xu SY, Belopolski I, Lee CC, Chang G, et al. 2015. *Nat. Commun.* 6:8373
21. Xu SY, Belopolski I, Alidoust N, Neupane M, Bian G, et al. 2015. *Science* 349:613
22. Lv BQ, Weng HM, Fu BB, Wang XP, Miao H, et al. 2015. *Phys. Rev. X* 5:031013
23. Yang LX, Liu ZK, Sun Y, Peng H, Yang HF, et al. 2015. *Nat. Phys.* 11:728–32
24. Murakami S. 2008. *New J. Phys.* 10:029802
25. Nielsen HB, Ninomiya M. 1981. *Nucl. Phys. B* 185:20–40
26. Nielsen HB, Ninomiya M. 1981. *Nucl. Phys. B* 193:173–94
27. Young SM, Zaheer S, Teo JCY, Kane CL, Mele EJ, Rappe AM. 2012. *Phys. Rev. Lett.* 108:140405
28. Wang Z, Sun Y, Chen XQ, Franchini C, Xu G, et al. 2012. *Phys. Rev. B* 85:195320
29. Wang Z, Weng H, Wu Q, Dai X, Fang Z. 2013. *Phys. Rev. B* 88:125427
30. Xu G, Weng H, Wang Z, Dai X, Fang Z. 2011. *Phys. Rev. Lett.* 107:186806
31. Yang KY, Lu YM, Ran Y. 2011. *Phys. Rev. B* 84:075129
32. Burkov AA, Balents L. 2011. *Phys. Rev. Lett.* 107:127205
33. Grushin AG. 2012. *Phys. Rev. D* 86:045001
34. Sun Y, Zhang Y, Felser C, Yan B. 2016. *Phys. Rev. Lett.* 117:146403
35. Adler SL. 1969. *Phys. Rev.* 177:2426–38
36. Bell JS, Jackiw R. 1969. *Nuovo Cim. A* 60:47–61
37. Nielsen HB, Ninomiya M. 1983. *Phys. Lett. B* 130:389–96
38. Son DT, Spivak BZ. 2013. *Phys. Rev. B* 88:104412
39. Parameswaran SA, Grover T, Abanin DA, Pesin DA, Vishwanath A. 2014. *Phys. Rev. X* 4:031035
40. Potter AC, Kimchi I, Vishwanath A. 2014. *Nat. Commun.* 5:5161
41. Baum Y, Berg E, Parameswaran SA, Stern A. 2015. *Phys. Rev. X* 5:041046
42. Bulmash D, Liu CX, Qi XL. 2014. *Phys. Rev. B* 89:081106(R)
43. Lu L, Wang Z, Ye D, Ran L, Fu L, et al. 2015. *Science* 349:622–24
44. Huang X, Zhao L, Long Y, Wang P, Chen D, et al. 2015. *Phys. Rev. X* 5:031023
45. Zhang CL, Xu SY, Belopolski I, Yuan Z, Lin Z, et al. 2016. *Nat. Commun.* 7:10735
46. Shekhar C, Nayak AK, Sun Y, Schmidt M, Nicklas M, et al. 2015. *Nat. Phys.* 11:645
47. Arnold F, Shekhar C, Wu SC, Sun Y, dos Reis RD, et al. 2016. *Nat. Commun.* 7:11615
48. Liu ZK, Zhou B, Zhang Y, Wang ZJ, Weng HM, et al. 2014. *Science* 343:864–67
49. Liu ZK, Jiang J, Zhou B, Wang ZJ, Zhang Y, et al. 2014. *Nat. Mater.* 13:677–81
50. Neupane M, Xu SY, Sankar R, Alidoust N, Bian G, et al. 2014. *Nat. Commun.* 5:3786
51. Borisenko S, Gibson Q, Evtushinsky D, Zabolotnyy V, Büchner B, Cava RJ. 2014. *Phys. Rev. Lett.* 113:027603
52. Soluyanov AA, Gresch D, Wang Z, Wu Q, Troyer M, et al. 2015. *Nature* 527:495–98
53. Sun Y, Wu SC, Ali MN, Felser C, Yan B. 2015. *Phys. Rev. B* 92:161107(R)
54. Liu ZK, Yang LX, Sun Y, Zhang T, Peng H, et al. 2016. *Nat. Mater.* 15:27–31
55. Sun Y, Wu SC, Yan B. 2015. *Phys. Rev. B* 92:115428
56. Lv BQ, Xu N, Weng HM, Ma JZ, Richard P, et al. 2015. *Nat. Phys.* 11:724–27
57. Xiao D, Chang MC, Niu Q. 2010. *Rev. Mod. Phys.* 82:1959–2007
58. Moll PJW, Nair NL, Helm T, Potter AC, Kimchi I, et al. 2016. *Nature* 535:266–70
59. Xu SY, Alidoust N, Belopolski I, Yuan Z, Bian G, et al. 2015. *Nat. Phys.* 11:748
60. Belopolski I, Xu SY, Sanchez DS, Chang G, Guo C, et al. 2016. *Phys. Rev. Lett.* 116:066802
61. Xu N, Weng HM, Lv BQ, Matt CE, Park J, et al. 2016. *Nat. Commun.* 7:11006

62. Souma S, Wang Z, Kotaka H, Sato T, Nakayama K, et al. 2016. *Phys. Rev. B* 93:161112
63. Lv BQ, Muff S, Qian T, Song ZD, Nie SM, et al. 2015. *Phys. Rev. Lett.* 115:217601
64. Xu SY, Belopolski I, Sanchez DS, Neupane M, Chang G, et al. 2016. *Phys. Rev. Lett.* 116:096801
65. Inoue H, Gyenis A, Wang Z, Li J, Oh SW, et al. 2016. *Science* 351:1184–87
66. Batabyal R, Morali N, Avraham N, Sun Y, Schmidt M, et al. 2016. *Sci. Adv.* 2:e1600709
67. Kourtis S, Li J, Wang Z, Yazdani A, Bernevig BA. 2016. *Phys. Rev. B* 93:041109
68. Kim HJ, Kim KS, Wang JF, Sasaki M, Satoh N, et al. 2013. *Phys. Rev. Lett.* 111:246603
69. Li Q, Kharzeev DE, Zhang C, Huang Y, Pletikosic I, et al. 2016. *Nat. Phys.* 12:550–54
70. Xiong J, Kushwaha SK, Liang T, Krizan JW, Hirschberger M, et al. 2015. *Science* 350:413–16
71. Li H, He H, Lu HZ, Zhang H, Liu H, et al. 2016. *Nat. Commun.* 7:10301
72. Wang Z, Zheng Y, Shen Z, Zhou Y, Yang X, et al. 2016. *Phys. Rev. B* 93:121112
73. Yoshida K. 1976. *J. Phys. Soc. Jpn.* 40:1027
74. Goswami P, Pixley JH, Das Sarma S. 2015. *Phys. Rev. B* 92:075205
75. Chang MC, Yang MF. 2015. *Phys. Rev. B* 92:205201
76. Ma J, Pesin D. 2015. *Phys. Rev. B* 92:235205
77. Zhong S, Moore JE, Souza I. 2016. *Phys. Rev. Lett.* 116:077201
78. Arnold F, Naumann M, Wu SC, Sun Y, Schmidt M, et al. 2016. *Phys. Rev. Lett.* 117:146401
79. Klotz J, Wu SC, Shekhar C, Sun Y, Schmidt M, et al. 2016. *Phys. Rev. B* 93:121105
80. Luo Y, Ghimire NJ, Bauer ED, Thompson JD, Ronning F. 2016. *J. Phys. Condens. Matter* 28:055502
81. dos Reis RD, Wu SC, Sun Y, Ajeesh MO, Shekhar C, et al. 2016. *Phys. Rev. B* 93:205102
82. Liang T, Gibson Q, Ali MN, Liu M, Cava RJ, Ong NP. 2014. *Nat. Mater.* 14:280–84
83. Narayanan A, Watson MD, Blake SF, Bruyant N. 2015. *Phys. Rev. Lett.* 114:117201
84. Parkin S, Jiang X, Kaiser C, Panchula A, Roche K, Samant M. 2003. *Proc. IEEE* 91:661–80
85. Singleton J. 2001. *Band Theory and Electronic Properties of Solids*. Oxford, UK: Oxford Univ. Press
86. Ghimire NJ, Luo Y, Neupane M, Williams DJ, Bauer ED, Ronning F. 2015. *J. Phys. Condens. Matter* 27:152201
87. Luo Y, Ghimire NJ, Wartenbe M, Choi H, Neupane M, et al. 2015. *Phys. Rev. B* 92:205134
88. Moll PJW, Potter AC, Ramshaw B, Modic K, Riggs S, et al. 2016. *Nat. Commun.* 7:12492
89. Chang TR, Chang G, Lee CC, Huang SM, Wang B, et al. 2016. *Nat. Commun.* 7:1–9
90. Wang Z, Gresch D, Soluyanov AA, Xie W, Kushwaha S, et al. 2016. *Phys. Rev. Lett.* 117:056805
91. Huang L, McCormick TM, Ochi M, Zhao Z, Suzuki M-T, et al. 2016. *Nat. Mater.* 15:1155–60
92. Deng K, Wan G, Deng P, Zhang K, Ding S, et al. 2016. *Nat. Phys.* 12:1105–10
93. Jiang J, Liu ZK, Sun Y, Yang HF, Rajamathi R, et al. 2016. arXiv:1604.00139
94. Liang A, Huang J, Nie S, Ding Y, Gao Q, et al. 2016. arXiv:1604.01706
95. Bruno FY, Tamai A, Wu QS, Cucchi I, Barreteau C, et al. 2016. *Phys. Rev. B* 94:121112(R)
96. Wang C, Zhang Y, Huang J, Nie S, Liu G, et al. 2016. arXiv:1604.04218
97. Wu Y, Jo NH, Mou D, Huang L, Bud'ko SL, et al. 2016. *Phys. Rev. B* 94:121113
98. Ali MN, Xiong J, Flynn S, Tao J, Gibson QD, et al. 2014. *Nature* 514:205–8
99. Muechler L, Alexandradinata A, Neupert T, Car R. 2016. arXiv:1604.01398
100. Keum DH, Cho S, Kim JH, Choe DH, Sung HJ, et al. 2015. *Nat. Phys.* 11:482–86
101. Qi Y, Naumov PG, Ali MN, Rajamathi CR, Schnelle W, et al. 2016. *Nat. Commun.* 7:11038
102. Kang D, Zhou Y, Yi W, Yang C, Guo J, et al. 2015. *Nat. Commun.* 6:7804
103. Pan XC, Chen X, Liu H, Feng Y, Wei Z, et al. 2015. *Nat. Commun.* 6:7805
104. Graf T, Felser C, Parkin SSP. 2011. *Prog. Solid State Chem.* 39:1–50
105. Yan B, de Visser A. 2014. *MRS Bull.* 39:859–66
106. Canfield PC, Thompson JD, Beyermann WP, Lacerda A, Hundley MF, et al. 1991. *J. Appl. Phys.* 70:5800
107. Butch NP, Syers P, Kirshenbaum K, Hope AP, Paglione J. 2011. *Phys. Rev. B* 84:220504
108. Tafti F, Fujii T, Juneau-Fecteau A, de Cotret SR, Doiron-Leyraud N, et al. 2013. *Phys. Rev. B* 87:184504
109. Pan Y, Nikitin AM, Bay TV, Huang YK, Paulsen C, et al. 2013. *Europhys. Lett.* 104:27001
110. Nakajima Y, Hu R, Kirshenbaum K. 2015. *Sci. Adv.* 1:e1500242
111. Kim H, Wang K, Nakajima Y, Hu R, Ziemak S, et al. 2016. arXiv:1603.03375
112. Fisk Z, Canfield PC, Beyermann WP, Thompson JD, Hundley MF, et al. 1991. *Phys. Rev. Lett.* 67:3310–13

113. Fu L, Kane CL. 2008. *Phys. Rev. Lett.* 100:096407
114. Chadov S, Qi XL, Kübler J, Fecher GH, Felser C, Zhang SC. 2010. *Nat. Mater.* 9:541
115. Xiao D, Yao Y, Feng W, Wen J, Zhu W, et al. 2010. *Phys. Rev. Lett.* 105:096404
116. Lin H, Wray LA, Xia Y, Xu S, Jia S, et al. 2010. *Nat. Mater.* 9:546–49
117. Liu C, Lee Y, Kondo T, Mun ED, Caudle M, et al. 2011. *Phys. Rev. B* 83:205133
118. Wang W, Du Y, Xu G, Zhang X, Liu E, et al. 2013. *Sci. Rep.* 3:2181
119. Shekhar C, Kampert E, Foerster T, Yan B, Nayak AK, et al. 2015. arXiv:1502.00604
120. Liu Z, Yang L, Wu SC, Shekhar C, Jiang J, et al. 2016. *Nat. Commun.* 7:12924
121. Logan JA, Patel SJ, Harrington SD, Polley CM, Schultz BD, et al. 2016. *Nat. Commun.* 7:11993
122. Chu RL, Shan WY, Lu J, Shen SQ. 2011. *Phys. Rev. B* 83:075110
123. Bruene C, Liu CX, Novik EG, Hankiewicz EM, Buhmann H, et al. 2011. *Phys. Rev. Lett.* 106:126803
124. Wu SC, Yan B, Felser C. 2014. *Europhys. Lett.* 107:57006
125. Shekhar C, Nayak AK, Singh S, Kumar N, Wu SC, et al. 2016. arXiv:1604.01641
126. Kreyssig A, Kim MG, Kim JW, Pratt DK, Sauerbrei SM, et al. 2011. *Phys. Rev. B* 84:220408
127. Müller RA, Lee-Hone NR, Lapointe L, Ryan DH, Pereg-Barnea T, et al. 2014. *Phys. Rev. B* 90:041109
128. Müller RA, Desilets-Benoit A, Gauthier N, Lapointe L, Bianchi AD, et al. 2015. *Phys. Rev. B* 92:184432
129. Hirschberger M, Kushwaha S, Wang Z, Gibson Q, Liang S, et al. 2016. *Nat. Mater.* 15:1161–65
130. Wang Z, Vergniory MG, Kushwaha S, Hirschberger M, Chulkov EV, et al. 2016. arXiv:1603.00479
131. Ruan J, Jian SK, Yao H, Zhang H, Zhang SC, Xing D. 2016. *Nat. Commun.* 7:11136
132. Yan B, Müchler L, Felser C. 2012. *Phys. Rev. Lett.* 109:116406
133. Wang Z, Alexandradinata A, Cava RJ, Bernevig BA. 2016. *Nature* 532:189–94
134. Tang P, Zhou Q, Xu G, Zhang SC. 2016. *Nat. Phys.* 12:1100–4
135. Nakatsuji S, Kiyohara N, Higo T. 2015. *Nature* 527:212–15
136. Nayak AK, Fischer JE, Sun Y, Yan B, Karel J, et al. 2016. *Sci. Adv.* 2:e1501870
137. Yang H, Sun Y, Zhang Y, Shi W-J, Parkin SSP, Yan B. 2016. arXiv:1608.03404
138. Schoop LM, Ali MN, Straßer C, Topp A, Varykhalov A, et al. 2016. *Nat. Commun.* 7:11696
139. Xu SY, Alidoust N, Chang G, Lu H, Singh B, et al. 2016. arXiv:1603.07318
140. Sinova J, Valenzuela SO, Wunderlich J, Back C, Jungwirth T. 2015. *Rev. Mod. Phys.* 87:1213
141. Müchler L, Zhang H, Chadov S, Yan B, Casper F, et al. 2012. *Angew. Chem.* 124:7333–37
142. Kong D, Cui Y. 2011. *Nat. Chem* 3:845–49
143. Chen H, Zhu W, Xiao D, Zhang Z. 2011. *Phys. Rev. Lett.* 107:056804
144. Xiao J, Kou L, Yam CY, Frauenheim T, Yan B. 2015. *ACS Catal.* 5:7063–67
145. Yan B, Stadtmüller B, Haag N, Jakobs S, Seidel J, et al. 2015. *Nat. Commun.* 6:10167

Annual Review of Condensed Matter Physics

Volume 8, 2017

Contents

Errata

An online log of corrections to *Annual Review of Condensed Matter Physics* articles may be found at http://www.annualreviews.org/errata/conmatphys